ROYAL SOCIETY
OF CHEMISTRY

The electronic properties of Au clusters on CeO$_2$ (110) surface with and without O-defects†

Arunabhiram Chutia, [ID] *[abc] David J. Willock [ID] *[d]
and C. Richard A. Catlow [ID] *[abd]

We use density functional theory with Hubbard corrections (DFT+U) to understand the local electronic properties of Au adatom and Au$_2$ dimer adsorption on the CeO$_2$ (110) surface. We show that, based on the initial geometries, we can observe Au species in a variety of charge states including Au$^+$, Au$^-$, Au$^{\delta-}$ and Au$^{\delta+}$–Au$^{\delta-}$. We present a detailed discussion using Bader charge analysis and partial density of states to support our observations. We also discuss the influence of solvent on the adsorption of Au adatoms adsorbed on top of an O-vacancy, which shows interesting geometrical and electronic properties.

1. Introduction

Since the early work of Haruta on low temperature CO oxidation and on hydro-chlorination of ethylene to vinyl chloride by Hutchings using Au as catalyst, there has been widespread interest in understanding the catalytic properties of Au.[1–3] Over the years, it has been shown that Au nanoparticles on oxide supports such as CeO$_2$ have high catalytic activity in many important chemical reactions such as in PReferential OXidation of CO in the presence of H$_2$ (PROX) and for cleaning the hydrogen supply for fuel cells.[4] One of the key properties of CeO$_2$ is the possibility of reversible release and storage of lattice oxygen to which the success of Au/CeO$_2$ systems in heterogeneous catalysis has been widely attributed. Many previous studies have investigated Au/CeO$_2$ catalysts. For example, Zhang *et al.* reported cationic Au species during CO oxidation at room temperature over a Au/CeO$_2$

[a]UK Catalysis Hub, RCaH, Rutherford Appleton Laboratory, Didcot, OX11 0FA, UK

[b]Department of Chemistry, University College London, Gordon Street, London, WC1H 0AJ, UK. E-mail: c.r.a. catlow@ucl.ac.uk

[c]School of Chemistry, University of Lincoln, Brayford Pool, Lincoln, Lincolnshire, LN6 7TS, UK. E-mail: achutia@lincoln.ac.uk

[d]Cardiff Catalysis Institute, School of Chemistry, Cardiff University, Cardiff, CF10 3AT, UK. E-mail: willockdj@cardiff.ac.uk

catalyst. They also studied the effect of humidity on catalyst activity.[5] Zhou et al. showed that the CO oxidation rate scales with the Au/CeO_2 interfacial length in Au/CeO_2 nanotowers.[6] Wang et al. used synchrotron-based in situ time resolved X-ray diffraction and X-ray absorption spectroscopies to analyse the catalytic behaviour of nanostructured $\{Au + AuO_x\}$–CeO_2 catalysts during the water-gas shift reaction. In this study they proposed that the $Au^{\delta+}$ species is not responsible for this reaction at high temperature.[7] The importance of various charged Au species on the CeO_2 surface has also been reported by many other workers. Li et al. showed, using in situ FTIR combined with HRTEM, TGA, CO-TPD, O_2-TPO and O_2-TPD experiments, that $Au^{\delta+}$ species are a prerequisite for the formation of formate and carbonate-like species during CO-oxidation at ambient temperature and in the presence of ultra-low-gold-loaded catalysts.[8] In an interesting study, related to the deactivation of an Au/CeO_2 catalyst during the low temperature water-gas shift reaction, Karpenko et al. showed the significance of Au^{n+} and Ce^{3+} species and concluded that the catalyst is dominated by the formation of stable adsorbed carbonate species and catalyst redox processes are less significant.[9] Experimental comparative studies of Au with other metals such as Cu, Pt and Ir on CeO_2 surfaces have also been reported.[10,11] Scirè et al. suggested that Au/CeO_2 catalysts for the PROX reaction could be affected by the oxidation state of Au, which has a significant role in the CO activation energy.[12] They also concluded that, in the case of Cu/CeO_2, the performance is significantly influenced by the CeO_2 morphology/reactivity. Furthermore, comparative studies on the interaction of Au on different surfaces such as CeO_2 and Fe_2O_3 have shown that well dispersed metallic Au nanoparticles can provide active sites for the low temperature CO oxidation reaction on both CeO_2 and Fe_2O_3.[13]

In addition to the above experimental studies, there have been numerous theoretical studies of Au on CeO_2 surfaces. For example, Camellone et al. concluded that the charged Au ions such as Au^+ and Au^{3+} activate molecular CO and its oxidation to CO_2. They predicted that the reactivity of Au nanoparticles nucleated at O vacancies can be recovered for cluster sizes as small as Au_2.[14] For this study they employed density functional theory (DFT) calculations with the Hubbard correction, which is commonly referred to as DFT+U. In their study, they used a U value of 4.5 eV for Ce ions with the Perdew–Burke–Ernzerhof (PBE) exchange and correlation functional. All the calculations were performed using periodic boundary conditions employing the Quantum ESPRESSO package. Chen et al. found that the Au adatom adsorption on CeO_2 (111) and CeO_2 (110) has the stability order of E_{ad} (Ce-vacancy) < E_{ad} (O-vacancy) < E_{ad} (stoichiometric surface).[15] In this study they used DFT+U with a U value of 5.0 eV for Ce and employed SIESTA and VASP code using PBE and BLYP exchange and correlation functionals. Murgida et al. used DFT+U with a U value of 4.5 eV for Ce and the PBE exchange and correlation functional employing VASP to address the crucial question of whether vacancies agglomerate or repel each other.[16] They showed that the energetically most stable near-surface oxygen vacancy structures for a broad range of vacancy concentrations have all vacancies at subsurface oxygen sites. In another interesting study, Zhang et al. investigated the adsorption of an Au atom on O-vacancy sites and proposed that O-vacancies and O-vacancy clusters could also be anchoring sites for Au nucleation.[17a] For this study they used DFT+U, with a U value of 5.0 eV for Ce. Hernandez et al. reported the electronic structure of Au adatom on CeO_2 (111) surface. In this work they showed that Au adatom can

adopt Au^0, Au^+ and Au^- electronic configuration. In the studies by Branda *et al.* a series of U values were explored for LDA+U and GGA+U and explained the interesting interplay of the Au^0/Au^+ (Ce^{4+}/Ce^{3+}) states. However, in these studies the influence of solvent molecules and cluster size effects on the electronic properties of Au/CeO$_2$ systems were not taken into account.[17a-c] In one of our recent studies we used DFT+U in conjunction with extended X-ray absorption fine structure (EXAFS) experiments on the geometrical and local electronic properties of Cu adatoms and Cu(II) ions in the presence of water molecules and of CuO nanoclusters on the CeO$_2$ (110) surface. In this study we also used a U value of 5.0 eV for the Ce ion species.[18]

Despite this extensive range of experimental and computational studies of the interaction of Au with the CeO$_2$ surface, there are considerable uncertainties in the nature and origin of various important cationic and anionic species displayed by Au on the surface of CeO$_2$. The current study therefore investigates the fundamental interactions of Au and Au$_2$ clusters on CeO$_2$ surface with and without O-vacancies using the DFT+U methodology. In the following section, we present the computational details followed by our results and discussion on Au adatom adsorption on CeO$_2$ (110) surface both with and without a surface O-vacancy; we also consider the effect of the presence of water molecules as a solvent phase. For these studies involving water molecules the dispersive effects might play a crucial role therefore, we used Grimme's dispersion correction (D3) method. We then extend our study to Au$_2$ clusters. Our results give new insights both into the interaction of Au with the surface of CeO$_2$ and the factors controlling the charge state of the adsorbed atoms.

2. Computational details

Our calculations used periodic boundary conditions employing the Vienna *Ab initio* Simulation Package (VASP) to perform all the spin-polarized DFT+U calculations.[19-21] Theoretical studies have shown that the stability of CeO$_2$ surfaces is in the order of (111) > (110) > (100); and it is generally considered that the CeO$_2$ (110) surface is catalytically more active.[22,23] Therefore, for our studies we have focused on the CeO$_2$ (110) surface. We used the projector augmented wave (PAW) method and the cut-off energy for the expansion of the plane-wave basis sets was set to 550 eV, which gave bulk energies converged to within 10^{-5} eV.[24] We chose a convergence criterion of 0.01 eV Å^{-1} for structural optimizations and a k-point grid of 4 × 4 × 1 was employed for all slab calculations. The Perdew–Burke–Ernzerhof (PBE) version of the generalized gradient approximation (GGA) was used to carry out geometry optimizations and total energy calculations.[25]

The ideal (110) surfaces were modeled by 2 × 2 and 3 × 3 cells. The slabs were cut from bulk CeO$_2$ with a calculated energy minimized lattice constant of 5.492 Å (which compares well with the experimental value of 5.411 Å) while in the direction perpendicular to the surface we used a vacuum gap of ~15 Å. For the initial 2 × 2 supercell calculations, we used 9 atomic layers; and in these models, we placed the Au atoms on both sides of the CeO$_2$ surface so as to nullify any spurious dipole moments that would be present in the single-sided system. For the calculations involving 3 × 3 systems, we used 5 atomic layers and the adsorption was allowed on only one of the two surfaces. Here the dipole moment, due to the adsorbed species, was taken into account by using the methods

implemented in VASP according to the procedures of Makov *et al.* and Neu-gebauer *et al.*[26,27] In our studies involving Au/CeO$_2$ (110) surface with an O-vacancy and water molecules, we have employed Grimme's dispersion correction (DFT+U+D3) as dispersive effects might be significant for such systems.[28]

Previous studies have reported that the localization of electrons in f-orbitals in Ce ions is correctly represented by the Hubbard parameter $U_{eff} = 5$ eV and following earlier works we also use this value in the present study.[17,18,23,29–31] The adsorption energy, E_{ad}, for species (X) placed on both sides of the slab was calculated as:

$$E_{ad} = \{E_{X+CeO_2} - (E_{CeO_2} + 2 \times E_X)\}/2, \tag{1}$$

where E_{X+CeO_2} is the energy of the system with the species X adsorbed in a symmetric fashion on the two CeO$_2$ (110) surfaces created in the slab model, with or without O-vacancies. E_{CeO_2} is the energy of the pristine CeO$_2$ (110) surface with or without O-vacancies. E_X is the energy of an isolated adsorbate, usually a single Au atom placed in an identical periodic cell to the full slab calculation. Vacancies and adsorbed species are included in symmetrically identical positions on each face of the slab model to ensure that no net dipole perpendicular to the surfaces is introduced. This became cumbersome for the solvated calculations and so in those calculations a single side of the slab was employed and a dipole correction perpendicular to the surfaces was used. In these cases eqn (1) was adapted by the removal of the factors of 2 when calculating the reported adsorption energies. In the case of slab models with symmetric inclusion of vacancies/adsorbates, the whole system was relaxed on geometry optimization. For the single surface cases, the three lower layers of the slab were frozen in their bulk optimized positions.

Charges on the various atoms were obtained using the Bader charge analysis as implemented by Henkelman and co-workers.[32] The charge density difference, ρ_{diff}, was calculated by subtracting the sum of the charge densities of the isolated adsorbate ρ_X and pristine geometry ($\rho_{Pristine\ surface}$) of the surface of the same geometry from the total charge density (ρ_{total}) of the system *i.e.*

$$\rho_{diff} = \rho_{total} - (\rho_{Pristine\ surface} + \rho_X) \tag{2}$$

We used the Visualization for Electronic and Structural Analysis (VESTA) package for the visualization of 3D and 2D charge density differences.[33,34]

3. Results and discussion

3.1. Adsorption of Au adatom on CeO$_2$ (110) surface

First, we investigate the geometrical and electronic properties of an adsorbed Au adatom in five surface site locations: (a) on top of an O atom (O$_{top}$), (b) on top of a Ce atom (Ce$_{top}$), (c) on the bridge between Ce and O atoms (O–Ce$_{bridge}$), (d) on the four-fold hollow site (4-fold hollow) and (e) long-bridge site (O···O$_{bridge}$) (see Fig. 1).

Geometries. The optimized structures are shown in Fig. 2. After relaxation of an Au adatom on top of a surface O atom (O$_{top}$), the Au atom moves to the long-bridge site (O···O$_{bridge}$, Fig. 1(e)). Similarly, relaxation of an Au adatom placed at
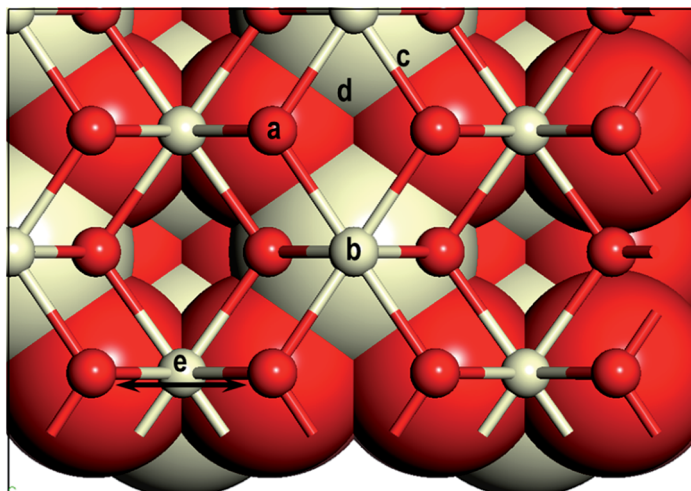
Fig. 1 Sites of Au adatom adsorption (a) on top of oxygen atom (O_{top}), (b) on top of cerium atom (Ce_{top}), (c) on the bridge between Ce and O atoms ($O-Ce_{bridge}$), (d) on the four-fold hollow site (4-fold hollow) and (e) on long-bridge site ($O\cdots O_{bridge}$).

the bridge site ($O-Ce_{bridge}$) results in the Au atom moving to the O_{top} site. Therefore, the former model can be referred to as the $O\cdots O_{bridge}$ model and the latter as the O_{top} model. On the other two sites, namely 4-fold hollow site and Ce_{top}, no such movements of the Au atoms are seen. As shown in Table 1, on calculating the various interatomic distances we find that the Ce–O distances on the exposed surfaces and in the bulk of the models are comparable with that of the pristine model. The Au–O distances display an interesting trend *i.e.*, $O\cdots O_{bridge}$ (2.132 Å and 2.171 Å) < $O-Ce_{top}$ (2.179 Å) << 4-fold hollow (2.655 Å) site, which suggests that Au interacts relatively strongly in the $O\cdots O_{bridge}$ model as compared to the other models. For the Ce_{top} model, the Ce–Au distance is 3.059 Å suggesting a very weak interaction between the Au and the Ce atom. Comparing to our earlier work, it is interesting to note that Au and Cu behave in a similar fashion when adsorbed on-top of an O atom, each moving to an $O\cdots O_{bridge}$ site.[18]
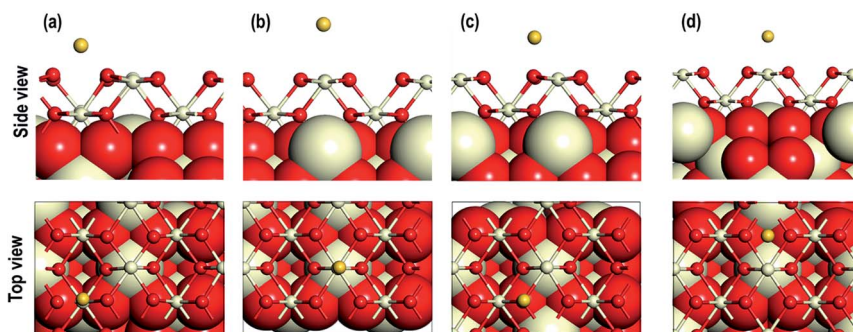

Fig. 2 Optimized side and top view of Au adatom adsorbed starting at the surface locations: (a) on $O\cdots O_{bridge}$, (b) on Ce_{top}, (c) on O_{top}, (d) 4-fold hollow sites.

Table 1 The average interatomic distances (in Å) for $(Ce-O)_{blk}$, $(Ce-O)_{srf}$, Au–O, Au–Ce and the adsorption energy (E_{ad}) in eV for the models with Au atom on different sites

System		Average interatomic distances (Å)				E_{ad} (eV)
		$(Ce-O)_{blk}$	$(Ce-O)_{srf}$	Au–O	Au–Ce	
Pristine		2.377	2.342	—	—	—
Au on	$O\cdots O_{bridge}$	2.378	2.327	2.132, 2.171	—	−1.132
	Ce_{top}	2.378	2.337	—	3.059	−0.332
	O_{top}	2.378	2.344	2.179	—	−0.977
	4-fold hollow	2.378	2.343	2.655	3.150	−0.684

However, in the $O-Ce_{bridge}$ case, we note that Au bonds with the nearest O atom, whereas a Cu adatom moves to the $O\cdots O_{bridge}$ site.[18] In the next section we present a detailed analysis of the electronic properties of the adsorbed configurations to gain insight into this behavior.
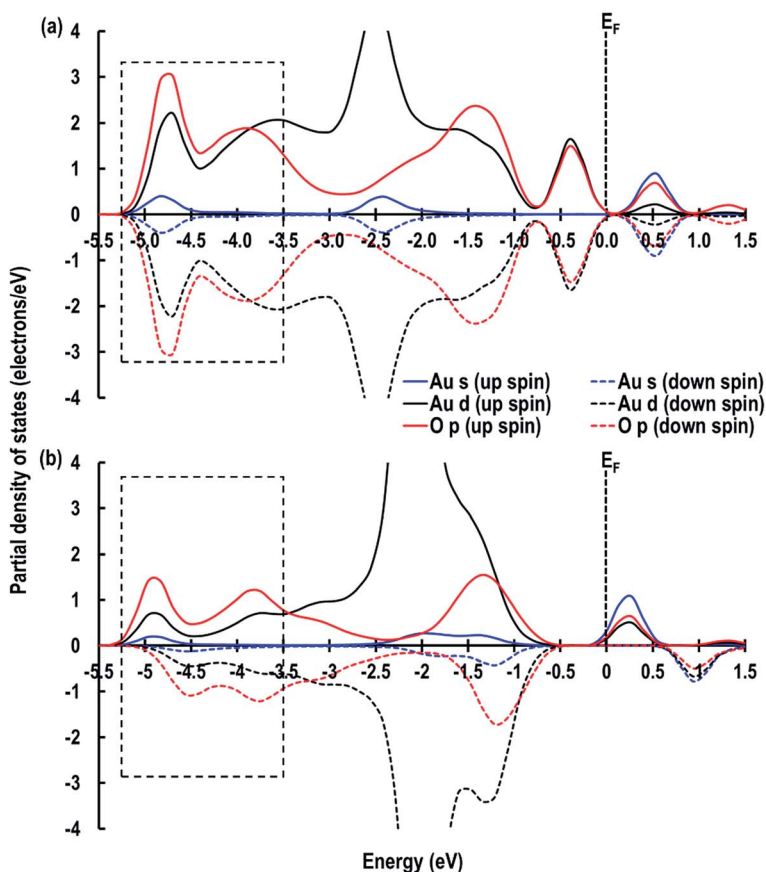

Fig. 3 Partial density of states for the (a) $O\cdots O_{bridge}$, (b) O_{top} systems. The Fermi energy (E_F) is shifted to zero and is marked by a dashed line.

Energetics of Au adsorption on the CeO$_2$ (110) surface. As shown in Table 1, the calculated adsorption energy (E_{ad}) is in the order of: O⋯O$_{bridge}$ (−1.132 eV) < O$_{top}$ (−0.977 eV) < 4-fold hollow (−0.684 eV) < Ce$_{top}$ (−0.332 eV) *i.e.*, the lowest energy site for an Au atom is the O⋯O$_{bridge}$ position. As mentioned in the previous section, in both O$_{top}$ and O–Ce$_{bridge}$ cases, the Au atom moves from its original position to the O⋯O$_{bridge}$ and O$_{top}$ sites, respectively, and the O⋯O$_{bridge}$ site is −0.155 eV lower in energy than the O$_{top}$ system. To help clarify the reason for this difference, we examine the partial density of states (PDOS), which shows that in the case of the O⋯O$_{bridge}$ system, the up and down-spin signatures due to the O p, Au (s and d) orbitals are symmetrical, but in the O$_{top}$ system, the up-spin and down-spin signatures are asymmetrical (Fig. 3(a and b)), which may be related to the fact that in the former case the O p-orbital signatures are due to Au interacting with two O atoms, while in the latter, only one O atom is involved. Furthermore, we also observe that around the Fermi energy (E_F) in the O⋯O$_{bridge}$ system, there is overlapping of the Au d-orbitals with the O p-orbital, which is absent for the O$_{top}$ system. In addition to it at around ∼−3.5 eV to ∼−5.3 eV (marked by rectangular box in Fig. 3) we can also see that the intensities of the overlapping O p and Au d orbitals are significantly higher for the O⋯O$_{bridge}$ system as compared to the O$_{top}$ system, which also clearly shows stronger inter-action between adsorbed Au atom with the CeO$_2$ surface in the former case.

Electron transfer between the Au atom and the CeO$_2$ (110) surface. Having studied the adsorption properties of the Au atom on the CeO$_2$ (110) surface, we then investigate the electron transfer between the Au atom and CeO$_2$ (110)
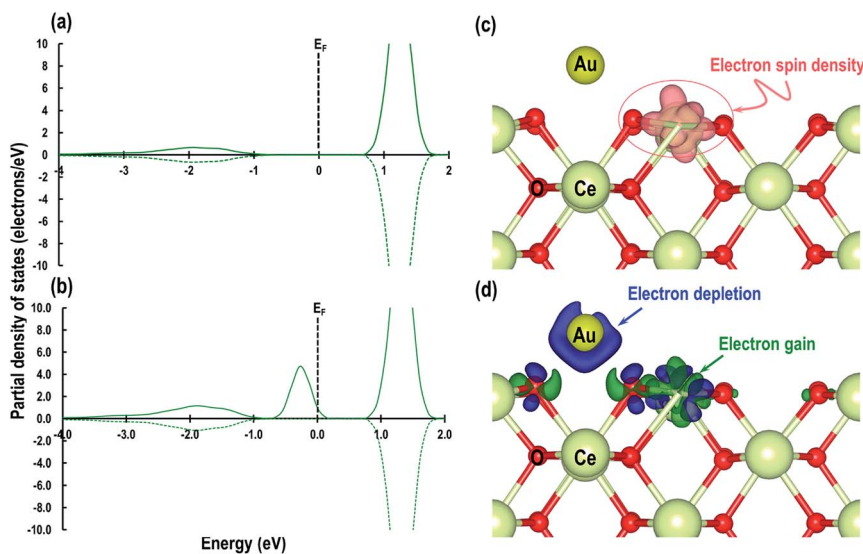

Fig. 4 Partial density of states of the surface Ce atom that is reduced on adsorption of Au; (a) on a pristine surface and (b) after reduction due to the adsorption of the Au atom. The Fermi energy (E_F) is shifted to zero and is marked by a dashed line, (c) electron spin density isosurface of 0.007 e Å^{-3} representing reduced Ce^{3+} cation and (d) electron charge density difference with an isosurface of 0.007 e Å^{-3} showing electron depletion around the Au atom in blue and electron gain in green on the Ce^{3+} cation.

surface. We compare the f-orbital contribution for a Ce atom in the pristine CeO_2 (110) surface with that of a Ce atom in the $O\cdots O_{bridge}$ system. As shown in Fig. 4(a and b), we find that in both cases there are traces of the f-orbital signatures from -3 eV to -1 eV; but after the adsorption of an Au atom on the CeO_2 (110) surface in the $O\cdots O_{bridge}$ system, the signature due to the f-orbital appears just below the fermi energy (E_F), showing the Ce^{4+} cation is reduced to Ce^{3+} due to electron transfer from the Au atom. We visualize the isosurface of electron spin density for the $O\cdots O_{bridge}$ model, which also displays electron gain by the reduced atom (Fig. 4(c)). We then visualize the electron charge density difference, which is calculated using:

$$\rho_{diff} = \rho_{(O\cdots O)_{bridge}} - (\rho_{Pristine\ CeO_2\ (110)\ surface} + \rho_{Au}), \qquad (3)$$

where ρ_{diff} is the charge density difference, $\rho_{(O\cdots O)_{bridge}}$ is the total charge density of the $O\cdots O_{bridge}$ system, $\rho_{Pristine\ CeO_2\ (110)\ surface}$ is the charge density of the $O\cdots O_{bridge}$ system without the Au atoms and ρ_{Au} is the charge density of the Au atoms in the gas phase. As shown in Fig. 4(d), we find electron depletion represented by the blue isosurface around the Au atom and electron gain around a Ce atom represented by the green isosurface. There are also some difference density features around two O atoms near the Au atoms, which may be related to the bonding interaction between the surface O atoms and the Au atom.

Furthermore, we also compare the Au s-orbital signatures of an Au atom in the gas phase with that of the adsorbed Au atom on the CeO_2 (110) surface (see Fig. S1
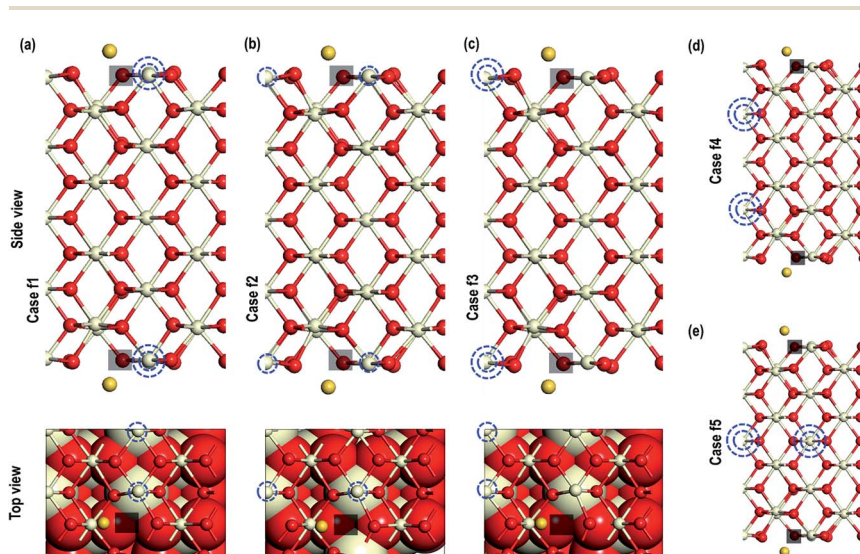

Fig. 5 Optimized structure of Au adatom adsorbed on top of an O-vacancy with the localisation of extra two electrons on (a) a Ce atom close to the O-vacancy another far (case 1), (b) a Ce atom close to the O-vacancy and another on the other side of the long-bridge (case 2), (c) two Ce atoms on the other side of the long-bridge (case 3), (d) two Ce with localisation in the second sub-surface (case 4) and (e) electron localised on the fifth sub-surface (case 5). The site of electron localisation is shown by blue dotted circles. For clarity the top and side views for first three cases are shown. The transparent black box represents the site of O-vacancies.

Table 2 The average (O–Ce)$_{srf}$ (distance between O and Ce on the surface), (O–Ce)$_{blk}$ (distance between O and Ce in the bulk), and O$_t$–Au (distance between surface O and Au adatom). The Bader charges on O, Ce^{4+}, Ce^{3+} (1), Ce^{3+} (2) and Au$^-$

	Average interatomic distances (Å)				Average Bader charges (e)				
System	(O–Ce)$_{srf}$	(O–Ce)$_{blk}$	(O–Au)$_{nearest}$	E_{ad} (eV)	O	Ce	Ce^{3+} (1)	Ce^{3+} (2)	Au
Case 1	2.364	2.373	2.340	−1.584	−1.198	2.385	2.059	2.113	−0.413
Case 2	2.394	2.381	2.157	−1.289	−1.198	2.380	2.047	2.094	−0.289
Case 3	2.376	2.379	2.305	−1.241	−1.198	2.377	2.108	2.121	−0.314
Case 4	2.347	2.380	2.305	−1.061	−1.198	2.369	2.218	2.220	−0.413
Case 5	2.359	2.380	2.152	−1.294	−1.198	2.368	2.098	2.240	−0.289
Case 6	2.321	2.378	2.978	−1.992	−1.194	2.376	2.053	—	−0.657

in ESI†) to confirm the loss of electron from the Au atom. From this comparison, we see that for the free Au atom, the up-spin Au s-orbital signature is just below the E_F while the down-spin signature is above it. After the adsorption of the Au adatom both up and down-spin signatures appear above E_F, which also confirms the transfer of the Au 6s^1 electron to the Ce atom to give an Au$^+$ species. Our results on Au$^+$ agrees well with those reported by Branda et al.[17c] The electron transfer phenomenon is finally illustrated by calculating the Bader charges, which give +2.383 e, −1.191 e and +0.263 e for Ce^{4+}, O^{2-} and Au$^+$ atoms, respectively, on the CeO$_2$ (110) surface. These calculated charges on O^{2-} and Ce^{4+} atoms accord with our previous studies on Cu/CeO$_2$ (110) surface,[18] i.e. +2.385 e for Ce, −1.196 e for O^{2-} atoms and +0.454 e for Cu^{1+} ions. The Bader charge on the reduced Ce atoms is seen to be +2.092 e confirming electron gain.
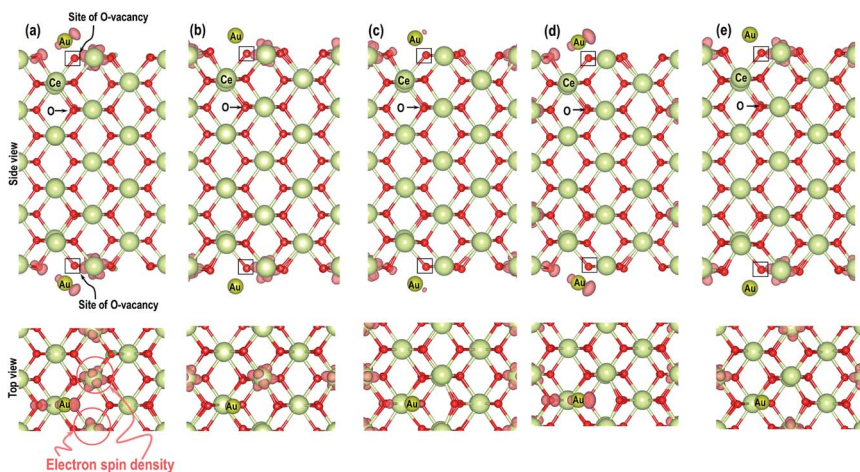

Fig. 6 Side and top views of electron spin density for the models (a) case 1, (b) case 2, (c) case 3, (d) case 4 and (e) case 5. The site of the O-vacancy is represented by an open black rectangular box and the pink lobe represents the electron spin densities with an isosurface of 0.007 e Å^{-3}.

Faraday Discussions

3.2. Adsorption of Au on the CeO$_2$ (110) surface with an O-vacancy

In the next step, we investigate the adsorption of Au on top of an O-vacancy in two steps *i.e.* we create an O-vacancy on the CeO$_2$ (110) surface and investigate the influence of the resulting reduced Ce atoms at different distances from the O-vacancy on the adsorption properties of Au. We note that previous work has shown that the lowest energy configuration of an oxygen vacancy in ceria involves reduction of neighbouring Ce ions and so these configurations are explored first, followed by a fully unconstrained minimisation.[35] The reduced Ce atoms are modelled next to the vacancy sites. The modelling of reduced Ce atoms in the various sites is effected by replacing the chosen Ce atoms with La atoms in the initial relaxation runs followed by full relaxation with the La atoms replaced again by the Ce atoms; a procedure shown previously to be effective in localising charge on the Ce.[17c,18] To avoid any spurious dipole moments, the oxygen vacancies were generated in symmetrically equivalent positions on both sides of the slab model. We will refer to these models as "Case *X*" (*X* = 1–5).

The optimized structures of the Au atom adsorbed on the top of an O-vacancy with the two extra electrons due to the O-vacancy localized on various Ce sites are shown in Fig. 5. In the figure, the localization sites of the electrons are shown with blue dotted lines. The calculated Au adsorption energy shows the following order: case 1 (−1.584 eV) < case 5 (−1.294 eV) < case 2 (−1.289 eV) < case 3 (−1.241 eV) < case 4 (−1.061 eV). On the optimized structures, we analyze the geometry and
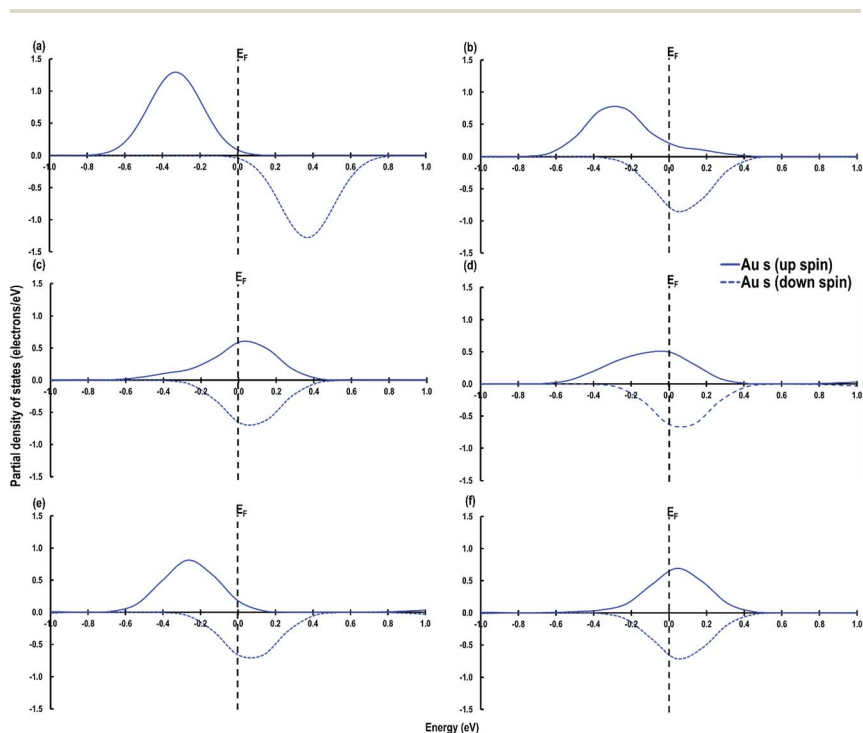

Fig. 7 Au s-orbital signatures for (a) Au atom in the gas phase, (b) case 1, (c) case 2, (d) case 3, (e) case 4 and (f) case 5. The Fermi energy (*E*$_F$) is shown by a dashed line crossing through 0.

other electronic properties such as electron density and PDOS for Au atoms for all the cases (1–5). On monitoring the various interatomic distances such as the nearest Au–O, Ce–O on the surface and in the bulk, we find that the Ce–O distances on the surface and in the bulk are comparable (Table 2). The distance between Au–O, however, shows the expected trend, *i.e.* for the systems with the highest (most negative) adsorption energies (in cases 2 and 5) the Au–O distances are shorter than the rest (*i.e.*, in cases 1, 3, and 4).

As shown in Fig. 6, we visualize the electron spin density of all these systems, which shows that, except for case 4, we find that irrespective of where the electrons are initially localized, after full relaxation the reduced Ce atoms are located on the surface. From the spin density, we observe, as expected, that two Ce atoms are reduced per O-vacancy. We also find localization of spin density on the Au atoms as well, except for cases 2 and 5. We plot the PDOS of Au atoms and compare it with the PDOS of a single Au atom (Fig. 7(a)), which shows that the unoccupied states of Au 6s orbitals (down-spin signatures in Fig. 7) move slightly below the E_F, indicating accumulation of a small amount of charge on Au atoms *i.e.*, $Au^{\delta-}$. As shown in Table 2, the Bader charge on the Au atoms is in the range of -0.289 e to -0.413 e correlating well with our analysis of the PDOS. We note that when the Bader charge on the Au atom is more positive than -0.319 e (cases 2, 3 and 5), the up and down-spin Au s-orbitals both move towards the E_F. Furthermore, from the Bader charge analysis, we find that due to an O-vacancy, there are two types of reduced Ce atoms, which we refer to as Ce^{3+} (1) and Ce^{3+} (2). One of these Ce^{3+} atoms is relatively more positive than the other, although the difference in Bader charges between these two Ce atoms is more prominent in cases 1 and 5; but in cases 2 and 3, this difference is insignificant. The charges on the other O^{2-} and Ce^{4+} ions are approximately -1.197 e and $+2.385$ e, respectively. This analysis leads us to conclude that the adsorption of an Au adatom on top of an O-vacancy may result in one of the two Ce atoms being partially reduced, with the partial reduction of the Au adatom resulting in an $Au^{\delta-}$ species.

Next we relaxed fully a model of Au adsorbed on top of an O-vacancy without following the procedure for localizing the electrons left behind due to the O-vacancy, which we will refer to as case 6. Our calculation shows that for this model, the adsorption energy is -1.992 eV, which is higher than found in the other configurations and which means the adsorption of an Au atom on the top of an O-vacancy is more stable than the $O\cdots O_{bridge}$ of a pristine CeO_2 (110) surface. On the fully relaxed case 6 model we performed a detailed electronic structure study. We begin with the analysis of electron spin density from which, as shown in Fig. 8(a), we observe that on both the exposed surfaces, there is only one Ce atom with electron spin density. To clarify the electron transfer phenomenon on this system, we plot the PDOS of the adsorbed Au atom over the O-vacancy and of the reduced Ce. Unlike the PDOS for the s-orbital in an Au atom (ESI Fig. S1(a)†), the PDOS for the s-orbital signature for the Au adatom on top of the O-vacancy shows both the up-spin and down-spin signatures below the E_F, which is a clear indication of electron gain (see Fig. 8(b)). Similarly, a plot of the PDOS for the Ce atom with spin density also shows electron gain (see Fig. 8(c)). The average Bader charge on all the O^{2-} ions is -1.194 e and on all the Ce^{4+} ions is $+2.376$ e. The average Bader charges on the Au^- and the reduced Ce^{3+} ion are -0.657 e and $+2.053$ e, respectively, which is also a clear illustration of electron transfer to Au atoms and reduction of the Ce atoms due to the presence of an O-vacancy.
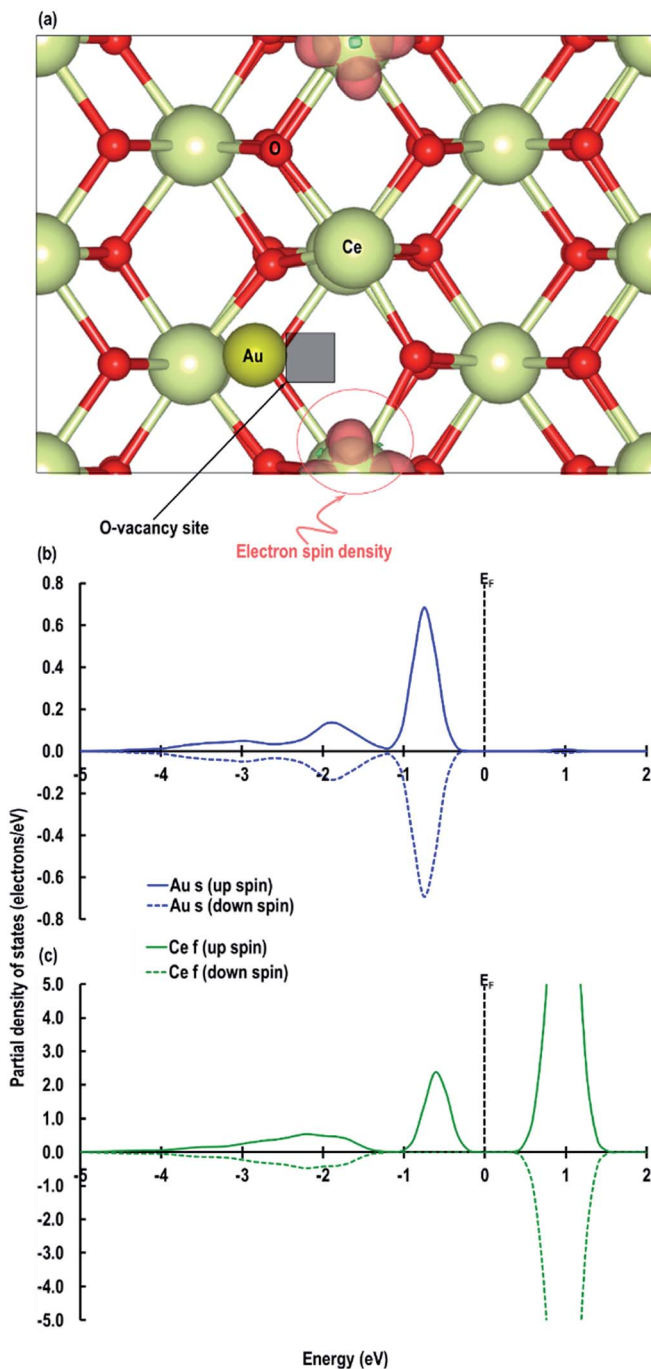
Fig. 8 (a) Electron spin density for the system of an Au atom adsorbed on top of an O-vacancy (shown as a black transparent box) without following the procedure for localising the electron (case 6), partial density of states (b) for the Au atom adsorbed on top of an O-vacancy and (c) for the reduced Ce on the CeO_2 (110) surface close to the O-vacancy.
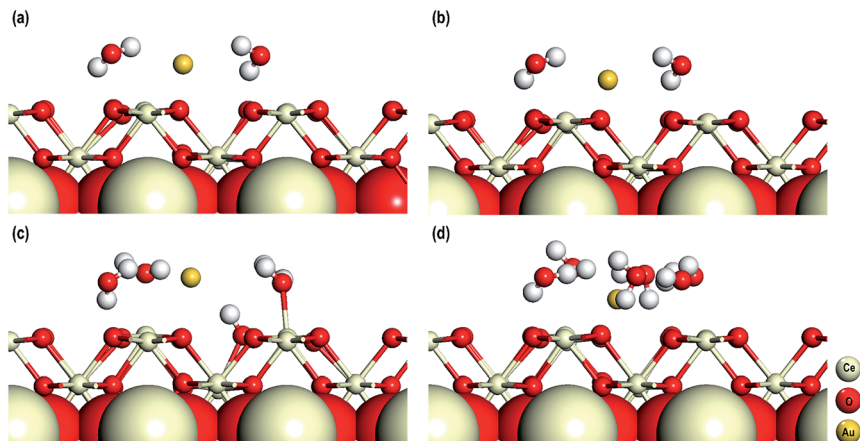
Fig. 9 (a) The optimized structures of the system with two water molecules at DFT+U level of theory. The optimized structures of the system with (b) two, (c) four and (d) six water molecules at DFT+U+D3 level of theory.

Previously Hernandez *et al.* also reported that Au adatom adsorbed close to an O-vacancy on CeO_2 (111) leads to Au$^-$ as well.[17b] We conclude that this configuration with a larger electron transfer to the Au and only one reduced Ce is the lowest energy state of Au absorbed over an oxygen vacancy, which in turn is lower in energy than adsorption on the pristine surface, although we note that alternative configurations involving two reduced Ce ions are close in energy indicating a complex electronic structure for this system.

Finally, we carried out a calculation on the adsorption of an Au adatom on top of an O-vacancy with five atomic layered CeO_2 (110) (3 × 3) surface model (CeO_2 $(110)_{3\times3}$ model). This calculation is performed in order to check the consistencies in results when we study the adsorption of Au adatom on top of an O-vacancy in

Table 3 The average (O–Ce)$_{srf}$ (distance between O and Ce on the surface), (O–H)$_{wat}$ (distance between O and H in the water molecules), O$_{wat}$–Ce$_{srf}$ (distance between O of water and Ce on the surface) and O$_{wat}$–Au (distance between O of water and Au adatom). The Bader charges on O, Ce^{4+}, Ce^{3+}, Au$^-$, O$_{wat}$ (O of water molecule) and H$_{wat}$ (H of water molecule)

System	Interatomic distances (Å)				Bader charges (e)					
	(O–Ce)$_{srf}$	O$_{wat}$–Au	(O–H)$_{wat}$	O$_{wat}$–Ce	O	Ce^{4+}	Ce^{3+}	Au$^-$	O$_{wat}$	H$_{wat}$
2 wat DFT+U	2.325	3.310	0.992	2.668	−1.178	2.349	2.193	−0.666	−1.261	0.612
2 wat DFT+U+D3	2.324	3.292	0.992	2.658	−1.178	2.347	2.227	−0.656	−1.276	0.619
4 wat DFT+U+D3	2.343	3.579	0.996	2.562	−1.179	2.357	2.070	−0.651	−1.265	0.606
6 wat DFT+U+D3	2.334	3.563	0.996	2.635	−1.179	2.356	2.073	−0.604	−1.256	0.611

the presence of water molecules only on one exposed surface of CeO$_2$ (110) models. The bottom three layers of the models are fixed to mimic the bulk of the CeO$_2$ (110) surface. We account for the dipole moment due to the adsorption of the Au atom on only one side of the two exposed surfaces by using the dipole correction methods as implemented in VASP according to the procedures of Makov *et al.* and Neugebauer *et al.* as mentioned in the computational details.[26,27] The average Bader charges on Ce^{4+}, Ce^{3+}, O and Au$^-$ species for the CeO$_2$ (110)$_{3\times3}$ model are +2.350 e, +2.050 e, −1.177 e and −0.674 e respectively. On analyzing other electronic properties such as electron spin density and PDOS of the reduced Ce atom we observe similar results to those discussed above, *i.e.*, reduction of a Ce^{4+} to Ce^{3+} cation and electron transfer to Au adatom giving Au$^-$ anion due to an O-vacancy (see Fig. S2 in the ESI†).

3.3. Adsorption of Au on the CeO$_2$ (110) surface with an O-vacancy in the presence of water

In the final stage of our study, we explore the influence of solvent molecules on their electronic properties on the adsorption of an Au adatom on the CeO$_2$ (110) surface in the presence of an O-vacancy. In addition to DFT+U, for these calculations we also use Grimme's D3 correction as with the inclusion of solvent molecules the dispersive effects might be important. These calculations are performed in the presence of 2, 4 and 6 water molecules and in all these systems an Au adatom is adsorbed on top of an O-vacancy. For these calculations we used five atomic layered CeO$_2$ (110) (3 × 3) surface models with the bottom three layers fixed to mimic the bulk of the CeO$_2$ (110) surface. The dipole moments are taken
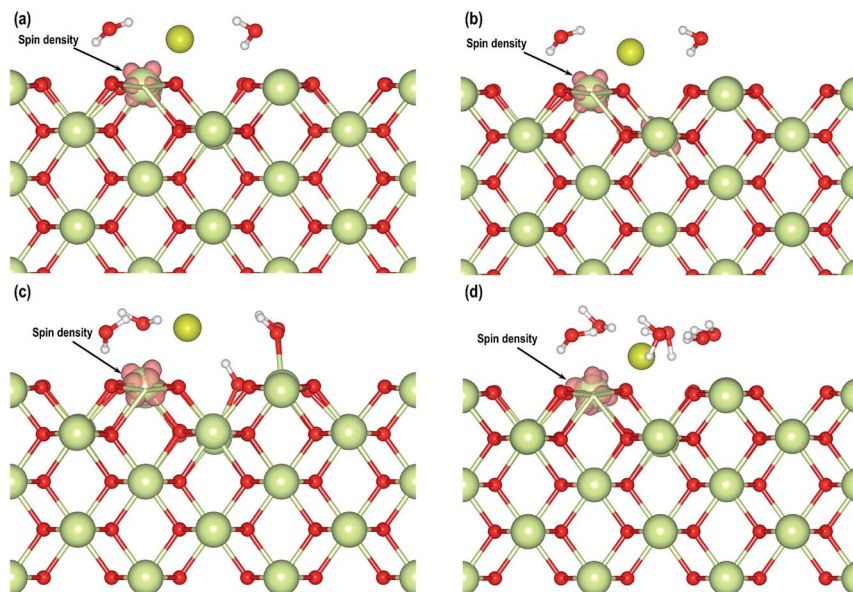

Fig. 10 (a) Electron spin density for model with two water molecules obtained by DFT+U calculations at an isosurface of 0.007 e Å^{-3}. Electron spin density for model with (b) two, (c) four and (d) six water molecules obtained by DFT+U+D3 calculations at an isosurface of 0.007 e Å^{-3}.

into account by considering the procedures of Makov *et al.* and Neugebauer *et al.* as mentioned in the computational details.[26,27] The optimized structures of these models are shown in Fig. 9.

The average $(O–Ce)_{srf}$, $(O–H)_{wat}$, $O_{wat}–Ce_{srf}$ and $O_{wat}–Au$ interatomic distances are first studied and we find that for all the models these distances are comparable. Interestingly, whether or not we use D3 corrections (for the models with two water molecules) these geometrical parameters are similar (see Fig. 9(a and b) and Table 3). In all the systems, we find that the water molecules arrange themselves in such a way as to form H-bonds either with the surface O atoms or among themselves. In the model with 4 water molecules, we also observe dissociation of one of the four water molecules. The dissociated water molecule is adsorbed on the surface forming a bond with the nearby Ce atom with an interatomic distance of 2.295 Å, which is comparable to the O–Ce distances on the surface (Table 3). The dissociated protonic hydrogen adsorbs on a nearby surface O atom with an interatomic distance of 0.993 Å, which is also comparable with the O–H distance in water molecules. No such dissociation of water molecules is seen in the other models.

After having considered the geometries of these systems, we also analyze the electron transfer with the help of Bader charges and partial density of states. In Table 3 we have summarized the Bader charges of different atoms from which we can observe that the average charges on O, Ce^{4+}, O_{wat} and H_{wat} atoms in all the models are comparable. We can also clearly see that in each of the models, one of the Ce atoms has a slightly lower positive charge compared with the Ce^{4+} atoms, indicating that the Ce^{4+} cations are reduced to Ce^{3+} cations due to the presence of the O-vacancy. The charges on the Au atoms also show electron gain. A visualization of the electron spin densities in all these models supports the reduction of one Ce atom (Fig. 10). Finally, we analyze the PDOS of the adsorbed Au s-orbital signatures and compare it with the Au in all the models. Both the up and down-
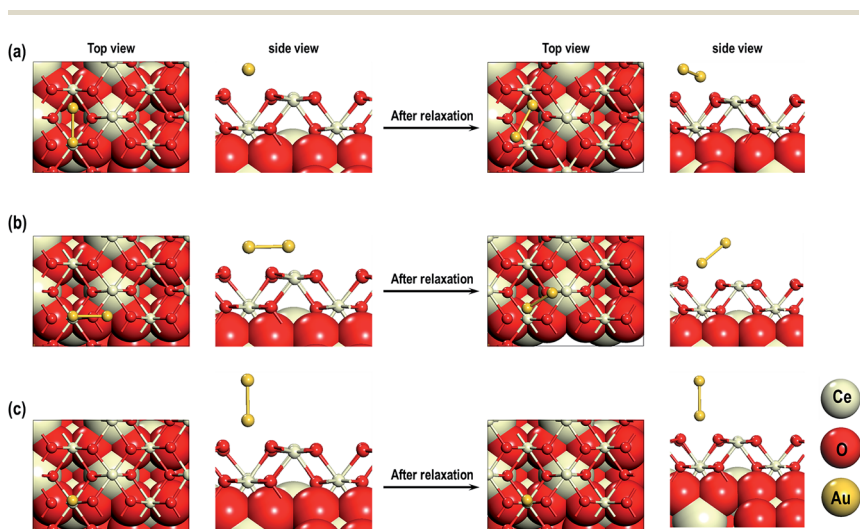

Fig. 11 Au_2 on (a) M_{Au-Dim} 1: one of the two Au atoms on the long-bridge site and another on the 4-fold$_{hollow}$ site, (b) M_{Au-Dim} 2: both the Au atoms on the long-bridge site and (c) M_{Au-Dim} 3: one of the two Au atoms is on the long-bridge site and the other above it.

Table 4 The average interatomic distances in Å, adsorption energies in eV and average Bader charges in units of e for the M_{Au-Dim} models

Systems	Average interatomic distances (Å)						Bader charge analysis (e)								
	Ce–O$_{srf}$	Ce–O$_{blk}$	(Au–O)$_a$	(Au–O)$_b$	Au–Au	E_{ad} (eV)	O	O (1)	O (2)	Ce	Au (1)	Au (2)	Ce^{3+} (1)	Ce^{3+} (2)	Ce^{3+} (3)
Au$_2$/CeO$_2$ (110)															
M_{Au-Dim} 1	2.356	2.377	2.139	2.089	2.588	−1.018	−1.191	−1.046	−1.101	2.384	0.017	0.050	2.174	—	—
M_{Au-Dim} 2	2.349	2.378	2.090 2.274	—	2.556	−1.237	−1.192	−1.084	−1.096	2.389	0.274	−0.308	2.232	—	—
M_{Au-Dim} 3	2.356	2.378	2.152 2.171	—	2.517	−1.039	−1.195	−1.095	−1.076	2.387	0.270	−0.214	2.159	—	—
Au$_2$/CeO$_2$ (110) with O-vacancy															
$M_{Au_2\_O\text{-vac}}$	2.383	2.378	2.028	—	2.546	−2.759	−1.200	—	—	2.380	0.004	−0.323	2.131	2.103	—

spin signatures due to Au s-orbitals are below the E_F confirming electron gain by the Au adatom leading to an Au$^-$ species (Fig. S3†). Furthermore, we compare the Bader charges on the CeO$_2$ (110)$_{3\times3}$ model without any water molecules (Section 3.2) and with two water molecules, which show that even though the charges on Ce^{4+}, O and Au$^-$ species are comparable, the charges on Ce^{3+} cations display slight differences, *i.e.* the charge on the reduced Ce^{3+} cation in the absence of two water molecules is +2.050 e while in the presence of two molecules it is +2.193 e. The difference in charge is +0.143 e, which may be attributed to the redistribution of charges due to the presence of water molecules.

From the above study on the adsorption of an Au adatom on top of an O-vacancy we conclude that, both in the presence and absence of water, such adsorption may led to two configurations with similar energies: first, an anionic metal atom (Au$^-$) with the reduction of a Ce^{4+} cation to Ce^{3+} cation, secondly, a fully reduced Ce^{3+} cation and a partially reduced Ce^{3+} cation with an Au$^{\delta-}$ species. In the next section, we extend our study to the Au$_2$ dimer on the CeO$_2$ (110) surface with and without an O-vacancy.

3.4. Adsorption of Au$_2$ on the CeO$_2$ (110) surface

Geometry and their stability. From our studies on Au adatom adsorption on the CeO$_2$ (110) surface, we saw that the Au adatoms are most stable on the long bridge site. Therefore, we use this structure to study the adsorption of an Au$_2$ dimer on the CeO$_2$ (110) surface. We consider three models *i.e.*, M$_{Au-Dim}$ 1: one of

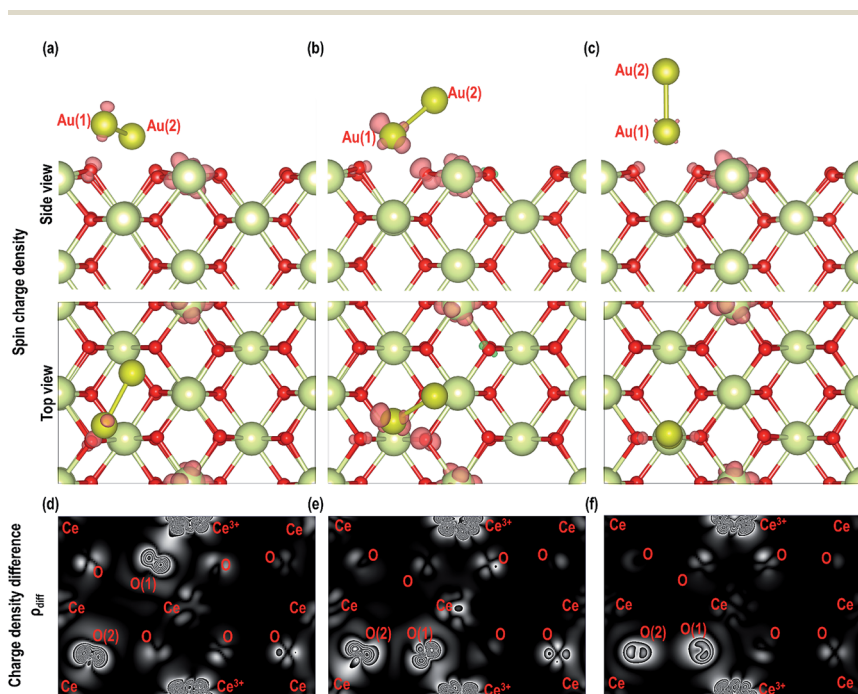Fig. 12 Top and side view of isosurface (0.007 e Å^{-3}) of spin densities of Au$_2$ on CeO$_2$ (110) surface for (a) M$_{Au-Dim}$ 1, (b) M$_{Au-Dim}$ 2 and (c) M$_{Au-Dim}$ 3 and 2D charge density difference contour maps of (d) M$_{Au-Dim}$ 1, (e) M$_{Au-Dim}$ 2 and (f) M$_{Au-Dim}$ 3.
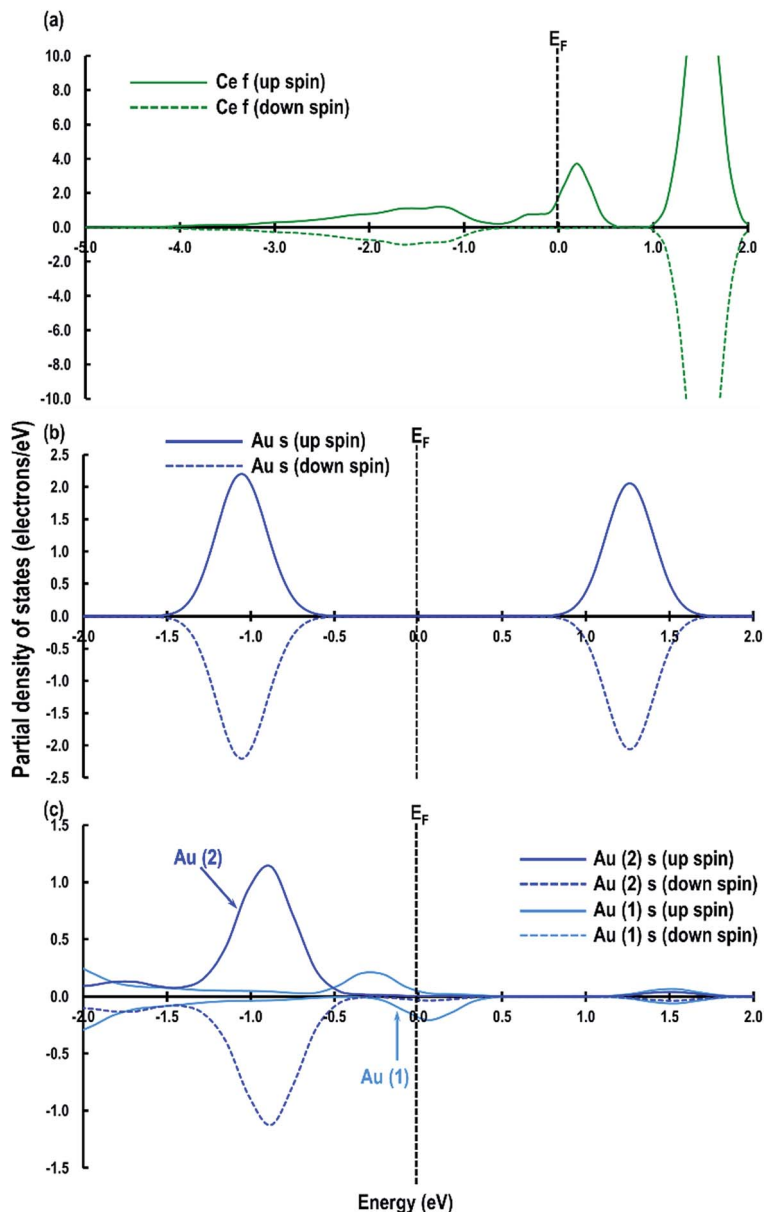
Fig. 13 Partial density of states for the (a) partially reduced Ce atom, (b) Au$_2$ dimer in the gas phase and (c) for the Au$_2$ in M$_{Au\text{-}Dim}$ 2 model. The E_F is moved to zero for convenience and is shown by a dotted line.

the two Au atoms on the long-bridge site and another on the 4-fold$_{hollow}$ site, M$_{Au\text{-}Dim}$ 2: both the Au atoms on the long-bridge site, and M$_{Au\text{-}Dim}$ 3: one of the two Au atoms is on the long-bridge site and the other above it. Fig. 11 shows the top and side view of the initial and the final structures. In models 1 and 2 we observe that one of the two Au atoms is closer to the surface, causing the Au dimer

to slant with respect to the surface. In the third model, the vertical geometry of the Au dimer relative to the surface does not change after relaxation. In M_{Au-Dim} 1, both the Au atoms are within the bonding distance from the surface O atoms with a distance of 2.089 Å and 2.139 Å. In the other two models, however, only one of the two Au atoms are within a bonding distance from a surface O atom. As shown in the Table 4, the Au–Au distances are comparable in all three models. The Ce–O distances on the surface and in the bulk, are also comparable to each other. The calculated adsorption energies show the following order: M_{Au-Dim} 2 (−1.237 eV) < M_{Au-Dim} 3 (−1.039 eV) < M_{Au-Dim} 1 (−1.018 eV), so model 2 has a lower energy than the other two models by approximately −0.20 eV.

Electronic structure. As shown in Fig. 12(a–c), we find that in all these models the spin densities (with an isosurface of 0.007 e Å^{-3}) are localized on one of the two Au atoms close to the surface and on two O atoms, which may be related to bonding between the Au and O atoms. In addition we note localization of spin densities around one Ce atom with the characteristics of the Ce f orbital, which may be linked to the reduction of the Ce atom. We also plot the 2D contour maps of charge density difference using the equation

$$\rho_{diff} = \rho_{Au_2+CeO_2\ (110)} - (\rho_{Pristine\ CeO_2\ (110)\ surface} + \rho_{Au_2}), \tag{4}$$

where ρ_{diff} is the charge density difference, $\rho_{Au_2+CeO_2\ (110)}$ is the total charge density of the Au$_2$/CeO$_2$ (110) system, $\rho_{Pristine\ CeO_2\ (110)\ surface}$ is the charge density of the CeO$_2$ (110) system without the Au$_2$ dimmer and ρ_{Au_2} is the charge density of the Au$_2$ in the gas phase. We plot 2D contours of ρ_{diff} for one of the two surfaces exposed to the Au$_2$ dimer, which also shows the localization of electrons around two O atoms (labelled as O (1) and O (2)) and a Ce atom (labelled as Ce^{3+}) (see Fig. 12(d–f)). The Bader analysis in Table 4 gives the average charges on the O atoms of ∼−1.193 e but on O (1) and O (2) the average charge is ∼−1.075 e and −1.091 e, respectively, showing that the O atoms closer to the Au share their electrons to form bonds with these nearby Au atoms.

We now investigate the electron transfer phenomenon in the M_{Au-Dim} 2 model which is the most stable structure among all three models considered in this study. The partial density of states for the Ce atom with localized spin density (as shown in Fig. 12(b)) is shown in Fig. 13(a). We observe that the Ce f-orbital signatures are beginning to populate around the E_F with a fraction of the signature just below it, indicating partial reduction. Our analysis of the Bader charges shows that the average charge on Ce atoms is +2.387 e and the charge on this Ce atom is +2.188 e, which shows that this Ce atom is partially reduced by the Au atoms closer to the surface, which have a charge of +0.274 e. It is also interesting to note that the Au atom further away from the surface (Au (2)) has a charge of −0.308 e. To clarify this observation, we make a comparative analysis of the PDOS for Au$_2$ dimer in the gas phase and Au$_2$ dimer adsorbed on the CeO$_2$ (110) surface in the M_{Au-Dim} 2 model (Fig. 13(b and c)). The PDOS for Au$_2$ dimer in the gas phase shows symmetrical up and down-spin signatures of Au s-orbitals above and below E_F. The two up and down-spin signatures below the E_F represent the occupied Au 6s^1 electrons from both the Au atoms of the Au$_2$ dimer. Similarly, the up and down-spin orbital signatures above the E_F

represent the unoccupied 6s-orbitals. It is clear that, unlike the PDOS for the Au atom (Fig. 7(a)), for the Au_2 dimer in Fig. 13(b) an energy gap appears between the highest occupied and lowest unoccupied orbitals. We then compared the Au s-orbital signatures from the Au atoms in the Au_2 in $M_{Au\text{-}Dim}$ 2 model. As shown in Fig. 13(c), the Au (2) atom, which is away from the surface, has prominent signatures for up and down-spin signatures below the E_F which are very small above the E_F, showing electron gain in Au (2). However, the Au (1) atom, which is closer to the surface, has asymmetric contribution from the Au s-orbital signature around the Fermi energy and a majority of the down-spin signature is above the E_F, which shows electron charge depletion on Au (1). Calculated Bader charges show that Au (1) and Au (2) have charges of $+0.274 \ e$ and $-0.308 \ e$, respectively, confirming our PDOS analysis. From this analysis, we find that Au (1) closer to the surface may share its electron partially with the other Au atom leading to a $Au^{\delta+}$–$Au^{\delta-}$-like system and may simultaneously partially reduce a Ce atom on the surface.

We now extend this study further to investigate the adsorption properties of Au_2 systems on the CeO_2 (110) surface with an O-vacancy on the surface, subsurface and in the bulk, which we present in the following section.
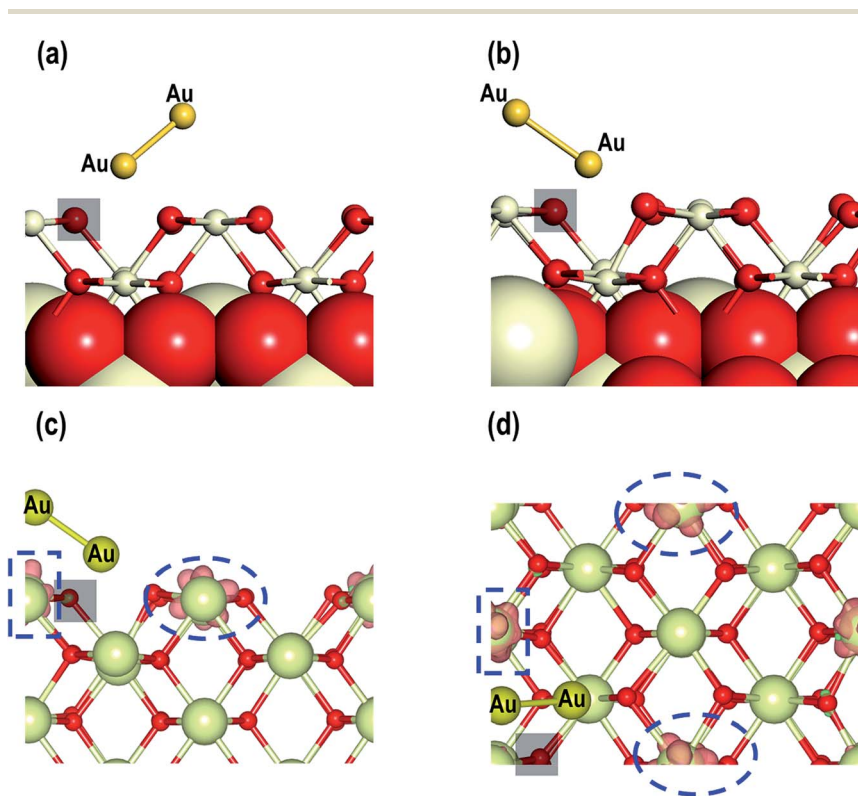

Fig. 14 (a) Initial and (b) final structure of the $M_{Au_2\_O\text{-}Vac}$ model. (c) Top and (d) side views of the isosurface ($0.007 \ e \ \text{Å}^{-3}$) of spin densities of the $M_{Au_2\_O\text{-}Vac}$ model. The transparent black rectangle represents an O-vacancy and the dotted circle and rectangle represent the isosurface ($0.007 \ e \ \text{Å}^{-3}$) of spin densities.

3.5. Adsorption of Au₂ on the CeO₂ (110) surface with an O-vacancy

For our studies on the adsorption properties of the Au_2 dimer in the presence of an O-vacancy we consider the most stable structure from the previous section and create an O-vacancy on the surface. We will refer to this model as $M_{Au_2\_O\text{-}Vac}$. The optimized structure for this model is shown in Fig. 14. There are minute contractions and expansions of bonds around the O-vacancy and near the Au_2 adsorbed sites. Various interatomic distances of this model are summarized in Table 4. The distance between O–Au is 2.028 Å. An important feature, noted in the relaxed geometry of this model is that, on relaxation, the Au_2 dimer on top of the O-vacancy changes its orientation to form a bond with a nearby O atom as shown in Fig. 14(a and b). The calculated adsorption energy shows that $M_{Au_2\_O\text{-}Vac}$ is the most stable system with a value of −2.759 eV (see Table 4). Like the Au/CeO_2 (110) in Au_2/CeO_2 (110) systems, we find that Au is most stable on top of an O-vacancy.

Finally, we analyze the electron transfer phenomenon and, as shown in Fig. 14(c and d), the visualization of the electron spin density shows that two Ce atoms are reduced. To quantify our observation on spin densities we calculated the Bader charges, which show that there are two reduced Ce^{3+} atoms *i.e.*, Ce^{3+} (1) with a Bader charge of +2.131 e and Ce^{3+} (2) with a Bader charge of +2.103 e (see Table 4). Like the $M_{Au\text{-}Dim}$ (1–3) models, for the $M_{Au_2\_O\text{-}Vac}$ model the Au atom that is closer to the surface *i.e.*, Au (1) in Table 4, has a slightly positive charge and the Au atom away from the surface Au (2) has a negative charge. From our studies on the adsorption of the Au_2 dimer on the CeO_2 (110) surface with and without O-vacancies we conclude that we observe $Au^{\delta+}$–$Au^{\delta-}$-like systems. On the CeO_2 (110) surface without an O-vacancy we show clear evidence of electron transfer from the Au_2 dimer but on the CeO_2 (110) surface with an O-vacancy we find reduction of Ce atoms rather than transfer to the Au.

4. Summary and conclusions

Our DFT+U calculations have revealed a range of interesting Au^+, Au^-, $Au^{\delta-}$ and $Au^{\delta+}$–$Au^{\delta-}$-like species on the CeO_2 (110) surface, as indicated by our analysis of partial density of states, electron spin densities, electron charge density differences and Bader charges. We conclude that the adsorption of an Au adatom will lead to Au^+ species due to electron transfer from Au to Ce; similarly the adsorption of an Au adatom on top of an O-vacancy will lead to Au^- species. However, if there is a partial reduction of a Ce atom on the surface of the CeO_2 (110) surface then we can see $Au^{\delta-}$ species. We also found that the adsorption of the Au-adatom on top of an O-vacancy is more stable than the pristine CeO_2 (110) surface. From our studies on the adsorption of the Au_2 dimer on the CeO_2 (110) surface we also draw similar conclusions that the Au_2 dimer is stable on top of an O-vacancy. Another significant point is that in Au_2/CeO_2 (110) systems, based on whether the Au atoms are closer or away from CeO_2 surface, there may be different electron loss or gain behaviour and we may observe unique $Au^{\delta+}$–$Au^{\delta-}$-like species. This study presents a detailed theoretical insight into the conditions under which we can observe the experimentally reported charged Au species. In addition to this it paves the way for further studies on the interaction of Au clusters with increasing size on the CeO_2 (110) surface with and without O-vacancies, which will lead to clearer understanding of the electron transfer phenomenon in such systems.

Acknowledgements

References

1 M. Haruta, T. Kobayashi, H. Sano and N. Yamada, *Chem. Lett.*, 1987, **16**, 405–408.

2 G. J. Hutchings, *J. Catal.*, 1985, **96**, 292–295.

3 A. S. K. Hashmi and G. J. Hutchings, *Angew. Chem., Int. Ed.*, 2006, **45**, 7896–7936.

4 M. Cargnello, C. Gentilini, T. Montini, E. Fonda, S. Mehraeen, M. Chi, M. Herrera-Collado, N. D. Browning, S. Polizzi, L. Pasquato and P. Fornasiero, *Chem. Mater.*, 2010, **22**, 4335–4345.

5 S. Zhang, X. S. Li, B. Chen, X. Zhu, C. Shi and A. M. Zhu, *ACS Catal.*, 2014, **4**, 3481–3489.

6 Z. Zhou, S. Kooi, M. Flytzani-Stephanopoulos and H. Saltsburg, *Adv. Funct. Mater.*, 2008, **18**, 2801–2807.

7 X. Wang, J. A. Rodriguez, J. C. Hanson, M. Pérez and J. Evans, *J. Chem. Phys.*, 2005, **123**, 221101.

8 Q. Li, W. Xie, G. Chen, Y. Li, Y. Huang and X. Chen, *Nano Res.*, 2015, **8**, 3075–3084.

9 A. Karpenko, R. Leppelt, J. Cai, V. Plzak, A. Chuvilin, U. Kaiser and R. J. Behm, *J. Catal.*, 2007, **250**, 139–150.

10 F. Pilger, A. Testino, M. A. Lucchini, A. Kambolis, M. Tarik, M. El Kazzi, Y. Arroyo, M. D. Rossell and C. Ludwig, *J. Nanosci. Nanotechnol.*, 2015, **15**, 3530–3539.

11 T. Akita, M. Okumura, K. Tanaka, M. Kohyama, S. Tsubota and M. Haruta, *J. Electron Microsc.*, 2005, **40**, 3101–3106.

12 S. Scirè, C. Crisafulli, P. M. Riccobene, G. Patanè and A. Pistone, *Appl. Catal., A*, 2012, **417–418**, 66–75.

13 W. Deng, C. Carpenter, N. Yi and M. Flytzani-Stephanopoulos, *Top. Catal.*, 2007, **44**, 199–208.

14 M. F. Camellone and S. Fabris, *J. Am. Chem. Soc.*, 2009, **131**, 10473–10483.

15 Y. Chen, P. Hu, M.-H. Lee and H. Wang, *Surf. Sci.*, 2008, **602**, 1736–1741.

16 G. E. Murgida and M. V. Ganduglia-Pirovano, *Phys. Rev. Lett.*, 2013, **110**, 1–5.

17 (*a*) C. Zhang, A. Michaelides, D. A. King and S. J. Jenkins, *J. Phys. Chem. C*, 2009, **113**, 6411–6417; (*b*) N. C. Hernandez, R. Grau-Crespo, N. H. de Leeuw and J. F. Sanz, *Phys. Chem. Chem. Phys.*, 2009, **11**, 5246–5252; (*c*) M. M. Branda, N. J. Castellani, R. Grau-Crespo, N. H. de Leeuw, N. C. Hernandez, J. F. Sanz, K. M. Neyman and F. Illas, *J. Chem. Phys.*, 2009, **131**, 094702.

18 A. Chutia, E. Gibson, M. R. Farrow, P. P. Wells, D. O. Scanlon, N. Dimitratos, D. J. Willock and C. R. A. Catlow, *Phys. Chem. Chem. Phys.*, 2017, **19**, 27191–27203.

19 G. Kresse and J. Hafner, *Phys. Rev. B*, 1993, **47**, 558–561.

20 G. Kresse and J. Hafner, *Phys. Rev. B*, 1994, **49**, 14251–14269.

21 G. Kresse and J. Furthmüller, *Phys. Rev. B*, 1996, **54**, 11169–11186.

22 L. Cui, Y. Tang, H. Zhang, L. G. Hector, C. Ouyang, S. Shi, H. Li and L. Chen, *Phys. Chem. Chem. Phys.*, 2012, **14**, 1923.

23 M. Nolan, S. Grigoleit, D. C. Sayle, S. C. Parker and G. W. Watson, *Surf. Sci.*, 2005, **576**, 217–229.

24 P. E. Blöchl, *Phys. Rev. B*, 1994, **50**, 17953–17979.

25 J. P. Perdew, K. Burke and M. Ernzerhof, *Phys. Rev. Lett.*, 1996, **77**, 3865–3868.

26 G. Makov and M. Payne, *Phys. Rev. B*, 1995, **51**, 4014–4022.

27 J. Neugebauer and M. Scheffler, *Phys. Rev. B*, 1992, **46**, 16067–16080.

28 S. Grimme, J. Antony, S. Ehrlich and H. Krieg, *J. Chem. Phys.*, 2010, **132**, 154104.

29 L. Szabová, M. F. Camellone, M. Huang, V. Matoln and S. Fabris, *J. Chem. Phys.*, 2010, **133**, 234705–11.

30 B. J. Morgan, D. O. Scanlon and G. W. Watson, *e-J. Surf. Sci. Nanotechnol.*, 2009, **7**, 389–394.

31 H. Raebiger, S. Lany and A. Zunger, *Phys. Rev. B*, 2007, **76**, 45209-1–45209-5.

32 W. Tang, E. Sanville and G. Henkelman, *J. Phys.: Condens. Matter*, 2009, **21**, 84204.

33 K. Momma and F. Izumi, *J. Appl. Crystallogr.*, 2011, **44**, 1272–1276.

34 K. Momma and F. Izumi, *J. Appl. Crystallogr.*, 2008, **41**, 653–658.

35 M. Nolan, S. C. Parker and G. W. Watson, *Surf. Sci.*, 2005, **595**, 223–232.